2007

Heating Methods and Detection Limits for Infrared Thermography Inspection of Fiber-Reinforced Polymer Composites

Jeff R. Brown
Hope College, browj112@erau.edu

H. R. Hamilton
University of Florida

ACI MATERIALS JOURNAL TECHNICAL PAPER

Title no. 104-M53

Heating Methods and Detection Limits for Infrared Thermography Inspection of Fiber-Reinforced Polymer Composites

by Jeff R. Brown and H. R. Hamilton

The use of fiber-reinforced polymer (FRP) composites to strengthen existing civil infrastructure is expanding rapidly. Many FRP systems used to strengthen reinforced concrete are applied using a wet lay-up method in which dry fibers are saturated on site and then applied to the surface. This research investigated using infrared thermography (IRT) as a nondestructive evaluation (NDE) tool for detecting air voids and epoxy-filled holes in FRP systems bonded to a concrete substrate. Four small-scale specimens with FRP thicknesses ranging from 1 to 4 mm (0.04 to 0.16 in.) containing fabricated defects were constructed and inspected in a laboratory setting. Three heating methods (flash, scan, and long pulse) were employed and a quantitative analysis of resulting IRT data was used to establish detection limits for each method. Scan heating was shown to be most effective for basic defect detection. Air-filled defects at the FRP/concrete interface as small as 2.9 cm^2 (0.45 in.^{2}) were detected in a 4 mm (0.16 in.) thick FRP system. Defects as small as 0.3 cm^2 (0.05 in.^{2}) were detected in a 1 mm (0.04 in.) thick FRP system.

Keywords: fiber-reinforced polymer composites; infrared thermography; nondestructive evaluation.

INTRODUCTION

Fiber-reinforced polymer (FRP) composites are currently used to repair and strengthen existing reinforced concrete (RC) structures. Flexural and shear strengthening require a strong mechanical bond between the applied FRP composite and the concrete substrate. The adhesive and concrete substrate must be sound and of sufficient strength to transfer stress to the fibers. The term "bond-critical" is often used to describe FRP strengthening because there are no redundant load paths for stress to follow should the bond fail.

If a composite is not installed properly and air bubbles are present at the FRP/concrete interface, the system may not perform as desired. In addition to affecting the ultimate strength of an FRP system, installation defects can also affect the overall durability of the system. Numerous researchers have cited durability of FRP composite systems as a major challenge confronting the FRP repair industry (CERF 2001; Kharbari et al. 2003; Nanni 2003). Factors that contribute to the degradation of an FRP composite system during its service life include environmental exposure (moisture and temperature cycles); overloading resulting in partial debonding; impact damage; and corrosion of internal reinforcing steel. After an extensive survey on defects in FRP composites, Kaiser and Kharbari (2001) concluded that the performance and expected lifetime of FRP repairs are largely dependent on the quality of installation and the presence of defects.

RESEARCH SIGNIFICANCE

The precise effect that defects have on the short- and long-term performance of FRP systems bonded to concrete is not well understood. The American Concrete Institute (ACI), the National Cooperative Highway Research Program (NCHRP), and International Congress of Building Officials (ICBO) have all recognized that defects are an important issue and have published guidelines describing allowable defect sizes in proportion to the total area of the FRP system (ACI Committee 440 2002; ICC Evaluation Services 2003; Mirmiran et al. 2004). All three published guidelines indicate that infrared thermography is a possible NDE technique for FRP systems. However, there are currently no specific guidelines describing how an IRT inspection should be performed for FRP systems used to strengthen concrete. This research seeks to provide additional experimental data that might be used in the formation of such guidelines.

BACKGROUND INFORMATION AND PREVIOUS RESEARCH

The fundamental concept behind using IRT as an NDE technique is to apply heat to the surface of an object and generate a thermal front that travels into the material. The increase in surface temperature should be uniform if the material is homogeneous. If the material contains defects below the surface, such as air voids, hot spots will develop because the flow of heat from the surface to the substrate is interrupted. These hot spots can be detected with an IR camera.

The aerospace industry has shown considerable interest in using IRT to inspect aircraft components constructed with FRP composite materials. Kulowitch, Perez, and Granata (1995) described efforts by the Naval Air Warfare Center to evaluate porosity and unbonded areas in graphite/epoxy laminates using pulse IRT. More recent work in the NDE/aerospace community has focused on obtaining quantitative information about the size and depth of defects in FRP composite systems. Maldague et al. (2002), Avdelidas et al. (2003), Bai and Wong (2001), and Carlomagno and Meola (2002) all applied numerical analysis techniques to IRT data in an effort to characterize defects. Recent research has also focused on data and image processing techniques that can be used to increase defect contrast and detectability in thermal images (Ibarra-Castenedo and Maldague 2005).

ACI Materials Journal, V. 104, No. 5, September-October 2007.
MS No. M-2006-283.R1 received July 19, 2006, and reviewed under Institute publication policies. Pertinent discussion including authors' closure, if any, will be published in the July-August 2008 *ACI Materials Journal* if the discussion is received by April 1, 2008.

Jeff R. Brown *is an Assistant Professor of engineering at Hope College, Holland, MI. His research interests include repair of corrosion damage in reinforced concrete structures, fiber-reinforced polymer composites, and nondestructive evaluation using infrared thermography.*

H. R. Hamilton *is an Associate Professor of civil engineering at the University of Florida, Gainesville, FL. His research interests include evaluation and strengthening of existing structures.*

Table 1—Material properties

Concrete mixture proportions	
Water-cement ratio (*w*/*c*)	0.45
Water, kg/m^3 (lb/yd^3)	217 (13.5)
Cement, kg/m^3 (lb/yd^3)	481 (30.0)
Fine aggregate, kg/m^3 (lb/yd^3)	700 (43.7)
Coarse aggregate, kg/m^3 (lb/yd^3)	902 (56.3)
Maximum aggregate size, mm (in.)	13 (0.51)
Dry fiber properties	
Area density, g/m^2 (oz/yd^2)	645 (19)
Tensile strength, MPa (ksi)	3790 (550)
Epoxy properties	
Glass transition temperature, °C (°F)	82 (181)
Tensile strength, MPa (ksi)	72.4 (10.5)
Lamina properties	
Thickness, mm (in.)	1 (0.04)
Tensile modulus, MPa (ksi)	82 (11.9)
Tensile strength, MPa (ksi)	834 (121)

Previous research has also been conducted on the IRT inspection of FRP composites used to strengthen RC. Levar and Hamilton (2003) conducted a study involving small-scale RC beams that were strengthened in flexure and shear using Carbon FRPs (CFRPs). These specimens were loaded to failure in a laboratory environment. IRT inspections were performed after the FRP systems were installed and areas that appeared unbonded in the thermal images were recorded directly on the specimen. IRT inspections were also performed at various stages of loading and patterns of debonding were monitored. Important observations from these experiments were as follows: the total debonded area increased as the load was increased up to failure, and certain debonded areas appeared to have different thermal signal strengths.

A study by Brown and Hamilton (2004) involved IRT inspections of full-scale AASHTO girders. Proprietary FRP strengthening systems (wet lay-up method) were applied to four AASHTO girders with simulated impact damage. The as-built thickness of these systems varied from 4 to 10 mm (0.16 to 0.39 in.), and a variety of fiber/matrix combinations were used (carbon/epoxy, carbon/polyurethane, and glass/vinylester). These girders were loaded to failure in a laboratory environment and IRT inspections were performed at various stages of loading. This study demonstrated the importance of properly calibrating the IRT inspection procedure with respect to surface heating and thermal image acquisition. The overall thickness of the FRP system, fiber and matrix type, and the procedure used to install the FRP system had a significant effect on IRT results.

Other important work on the IRT inspection of FRP applied to concrete was reported by Starnes et al. (2003). These studies included experimental work on a small-scale specimen with fabricated defects at the FRP/concrete interface. A single-layer precured carbon-epoxy laminate was bonded to a concrete substrate using an epoxy bonding agent. The total thickness of the laminate was 1.3 mm (0.05 in). A major focus of this work was to match experimental results with results from finite element models. Another study conducted by Starnes and Carino (2005) included estimating the planar size of defects using IRT results. It was shown that defect size can be accurately predicted by analyzing the surface temperature gradient caused by defects.

CURRENT RESEARCH OBJECTIVES

This research seeks to provide experimental data for the development of IRT inspection procedures and analysis techniques. The specific focus is to evaluate bond in FRP composites applied to concrete. The primary objectives may be summarized as follows:

- Determine the IRT detection limits for simulated defects in FRP composite systems ranging from 1 to 4 mm (0.04 to 0.16 in.) thick;
- Compare and validate three IRT inspection methods deemed suitable for field use; and
- Examine quantitative procedures that can be used to characterize the size and temperature versus time response of detected defects.

This paper contains results for carbon-epoxy FRP systems that were applied using a wet lay-up method. The primary variables that were studied included the thickness of the FRP composite, defect size, and defect composition (air filled versus epoxy filled). The three different heating methods investigated were: flash, scan, and long pulse. Flash heating experiments were conducted using a photographer's flash, whereas the scan and long-pulse heating experiments were conducted using 500 W halogen lamps.

EXPERIMENTAL SETUP AND DESIGN

Specimen construction

Four concrete blocks (30.5 x 15 x 5 cm [12 x 6 x 2 in.]) were cast using the mixture design provided in Table 1. This is a non-air-entrained mixture with a target slump of 7.6 to 10 cm (3 to 4 in). Steel plates were used as the bottom surface of the concrete formwork and a thin layer of form-release oil was applied to the surface of the steel before the concrete was placed. Prior to finishing, the concrete was consolidated in the formwork with a vibrating table. The concrete was allowed to cure in the forms for 2 days. No additional curing was provided after the forms were removed. Each specimen received a light sandblasting, and the FRP composite was applied to the surface of the block that had been in direct contact with the steel formwork.

Each of the four specimens contained a series of fabricated defects at the FRP/concrete interface. Defects were created by drilling a series of holes (three at 6.4 mm [0.25 in.], three at 12.7 mm [0.5 in.], and two at 19 mm [0.75 in.]) to a depth of 6.4 mm (0.25 in.) into the concrete substrate on the surface of each specimen. These defects were intended to simulate bug holes or other surface imperfections. It should be noted that small delaminations in which the bond between the FRP and concrete is broken may provide a different thermal response. Three of the holes (one of each diameter) were backfilled with thickened epoxy tack coat and two of the holes were backfilled with polyurethane insulating foam. The remaining three holes were left empty to represent air-filled defects (Fig. 1).

An interface bubble was also implanted in each specimen by inserting a small nylon machine screw (No. 8) into the

Table 2—Series A details

Specimen ID	FRP thickness, mm (in.)	Weight volume of fibers	Interface bubble	
			$d_{\|\|}$, mm (in.)	$d_{\perp}$, mm (in.)
A-1	1 (0.04)	0.50	51 (2.0)	18 (0.71)
A-2	2 (0.08)	0.50	57 (2.24)	29 (1.14)
A-3	3 (0.12)	0.50	57 (2.24)	25 (0.98)
A-4	4 (0.16)	0.50	51 (2.0)	32 (1.26)

surface of the concrete. The machine screw was cut such that it protruded 3 mm (0.12 in.) above the surface of the concrete before the FRP composite was applied. The final dimensions for each interface bubble were obtained by measuring the size on the surface of the cured composite. Two measurements were made: one parallel ($d_{\|}$) and one perpendicular ($d_{\perp}$) to the principle fiber direction (Table 2).

The carbon fiber and epoxy matrix used in this study were typical of those commonly used in wet lay-up FRP composites for strengthening RC (Table 1). Precured laminates were not addressed in this study. The dry carbon fibers were a unidirectional, stitched fabric with a thin veil of multidirectional glass fibers.

Specimens A-1, A-2, A-3, and A-4 were constructed using one, two, three, and four layers of carbon-fiber composite, respectively. Each specimen received a light sandblasting and a 10 cm (4 in.) wide velour paint roller was used to apply a thin layer of epoxy saturant to the concrete surface. The average amount of saturant used was 13.3 mg/cm^2 (3.9 oz/yd^2). The epoxy was allowed to sit on the surface for approximately 1 hour before a layer of thickened epoxy tack-coat (24.5 mg/cm^2 [7.2 oz/yd^2]) was applied using the same velour roller.

The hand-roller method was used to saturate all of the carbon fiber. The target fiber to matrix saturation level for each layer of composite was 1:1 by weight. This level was achieved by carefully adding epoxy and weighing the composite before and after the roller was used to saturate the fibers. The resulting weight volume fraction for each layer of the composite was 0.50. A final coat of epoxy was also applied as a top coat in accordance with the manufacturer's installation guidelines.

Thermal imaging system

An infrared camera was used in this study. This thermal-imaging system operates in the 8 to 12 μm (LWIR) wavelength band of the electromagnetic spectrum. An important feature of this camera is the ability to save thermal images digitally. Each pixel in the thermal image (320 x 240) is stored as a temperature value which allows for post-processing of collected images using proprietary software or Matlab. The maximum image save rate for this thermal imaging system is five frames per second (5 Hz).

Heating methods

An ideal heating method would generate a uniform heat flux across the entire surface area (*x-y* plane) within the field of view (FOV) of the IR camera. Nonuniform heating results in temperature gradients on the *x-y* plane that affect the overall signal generated by defects. Ultimately, the ability to generate uniform heating in the *x-y* plane is limited by the need to record thermal images during heating and the total area that must be heated simultaneously. The heating methods investigated in the current study were chosen because they represent likely candidates for field use.

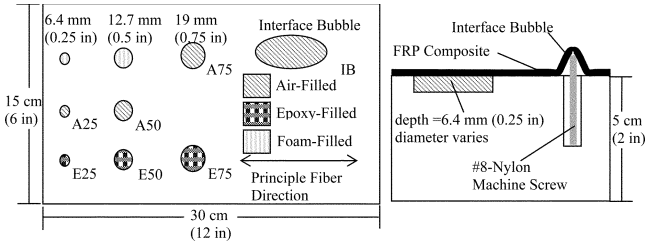

Fig. 1—Defect configuration for Series A specimens.

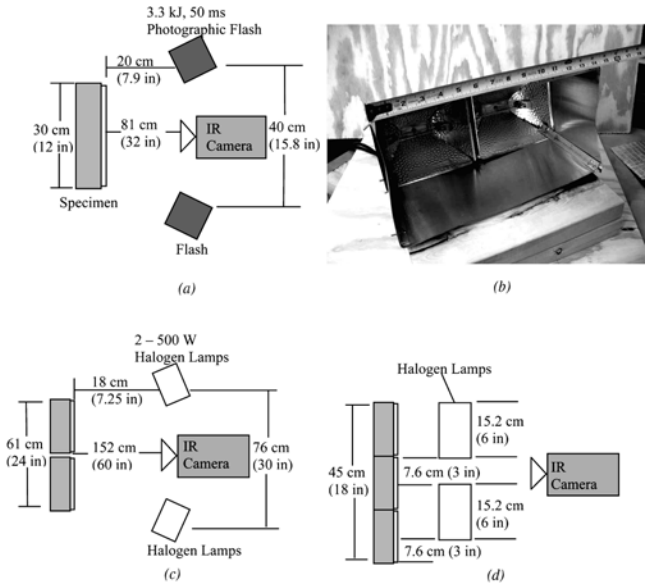

Fig. 2—Heat source and camera configurations: (a) flash heating (plan view); (b) scan heating; (c) long-pulse heating (plan view); and (d) long-pulse heating (profile view).

Flash heating experiments were conducted using two 3.3 kJ (3.13 BTU) photography flash systems (total energy rating = 6.6 kJ [6.26 BTU]). Each flash system consisted of a power pack and a lamp head. The total pulse duration was 50 ms. A 17.8 cm (7 in.) diameter reflector shield was used on each lamp head. The heat source and camera configuration used in the flash heating experiments is provided in Fig. 2(a). This configuration was chosen because it provided enough intensity to develop a signal for defects in the three- and four-layer FRP systems.

The general concept behind scan heating is that the heat source is moved across the surface of the composite at a constant rate and the IR camera is positioned to record the surface temperature as the specimen cools. The heat source developed for this study is shown in Fig. 2(b). Two 500 W halogen work lights were used as the energy source and the safety glass was removed. A thin heat shield was constructed using adhesive-backed sheet metal to help focus the energy from the lamps. The dimensions of the shield opening were 35.6 x 20.3 cm (14 x 8 in.) and the plane of the opening was offset a distance of 18.4 cm (7.25 in.) from the lamp bulb. During each experiment, the heat shield opening was held approximately 7.6 cm (3 in.) from the surface of the specimen. The heat source was moved from left to right at a constant rate of approximately 2.2 cm/s (0.87 in./s). The total amount of time that any one point on a specimen was exposed to the heat source was 12 seconds.

The long-pulse heating configuration is provided in Fig. 2(c) and (d). Four 500 W halogen lamps were used to provide a square heat pulse for a 30-, 45-, or 60-second pulse duration. The 500 W halogen lamps were similar to those used in the heat source for scan heating. The safety glass was left in place for the long-pulse heating setup to minimize the risk of ultraviolet (UV) exposure for the operator.

RESULTS AND ANALYSIS

Flash, scan, and long-pulse heating methods were used to inspect the small-scale specimens containing fabricated defects. Three pulse durations were considered for the long-pulse heating: 30, 45, and 60 seconds. Thermal images were saved at a rate of one frame per second during heating and then for an additional 240 seconds while the specimens cooled. Images collected during heating were not considered in the current analysis because these images contained reflected IR energy from the heat source. Additional research is ongoing to examine methods for using images gathered during heating.

Comparison of background surface temperature increase

A background surface temperature increase refers to the change in temperature that occurs in defect-free regions due to heating. Specimen A-1 was chosen as a reference, and the temperature profile was measured along a vertical (L1) and horizontal (L2) line passing through the center of the specimen

Table 3—Surface temperature increase results for different heating methods

Heating method	Total area heated, cm^2 ($in.^2$)	Horizontal profile (L2)		σ_{norm}, %	Vertical profile (L1)		σ_{norm}, %
		ΔT_{max}, °C (°F)	ΔT_{max}, °C (°F)		ΔT_{max}, °C (°F)	ΔT_{mean}, °C (°F)	
Flash	464 (72)	5.8 (10.4)	5.2 (9.4)	12.5	6.1 (11.0)	5.2 (9.4)	7.8
Scan	1858 (288)	NA	NA	NA	18.4 (33.1)	17.1 (30.8)	4.5
Long pulse (30 seconds)	2787 (432)	9.3 (16.7)	6.2 (11.2)	23.4	7.3 (13.1)	6.8 (12.2)	2.6
Long pulse (60 seconds)	2787 (432)	11.4 (20.5)	7.3 (13.1)	23.8	8.7 (15.7)	8.1 (14.6)	2.6

Note: NA = not available

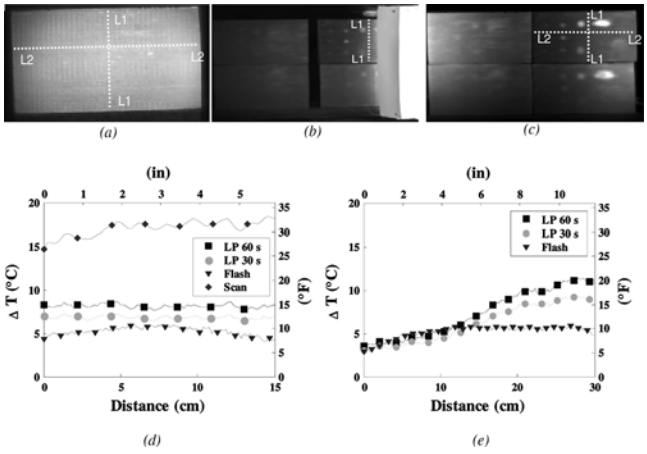

Fig. 3—Thermal images collected at end of heating for: (a) flash heating; (b) scan heating; and (c) long-pulse heating (60-second pulse duration); and temperature profiles for: (d) vertical line (L1); and (e) horizontal line (L2).

(Fig. 3). For scan heating, only the vertical line was reported because the heat source configuration blocked access to the horizontal profile during heating (Fig. 3(b)). The values for ΔT_{max} and ΔT_{mean} were obtained directly from each temperature profile and σ_{norm} was computed by taking the standard deviation of the normalized temperature increase (Table 3).

The scan heating method provided the largest mean surface temperature increase (ΔT_{mean} = 17.1 °C [30.8 °F]). This increase was also relatively uniform with respect to the vertical axis (σ_{norm} = 4.5% perpendicular to the direction of movement by the heat source). The major downside to this heating method is that surface under consideration is not heated at the same time. The rate at which the heat source is moved affects the magnitude of the temperature increase as well as the total duration of the heat pulse.

Long-pulse heating using halogen lamps was an effective means for heating a relatively large surface area simultaneously. Up to six specimens (2787 cm^2 [3 ft^2]) could be heated during each experiment, and it was possible to record thermal images during heating and cooling. This method did generate a large thermal gradient in the *x*-*y* plane with the largest temperature increase occurring closest to the lamps. For the 60-second pulse duration, the ratio of maximum to minimum temperature increase that occurred across Specimen A-1 was 2.77:1.

Finally, flash heating generated a mean surface temperature increase of 5.2 and 5.8 °C (9.4 and 10.4 °F) for the horizontal and vertical profiles, respectively. The major limitation encountered with flash heating was the relatively small area (464 cm^2 [0.5 ft^2]) that could be inspected each time the flash was fired (Fig. 3(a)).

DEFECT ANALYSIS

Defect signal strength

A quantitative analysis was performed for each implanted defect using a contrast-based approach. The value ΔT_{def} is defined as the difference in temperature between the defect area and the surrounding defect-free area. Two options were investigated for computing ΔT_{def} in a single thermal image:

- Select a single pixel above the defect and a single pixel adjacent to the defect (subtract the two values); and
- Identify small areas above the defect and adjacent to the defect and compute an average (subtract the two values).

The first method raises the issue of how the points should be selected for the defect and defect-free areas. The defect itself might occupy as many as 500 pixels in a typical thermal image. The location of the maximum value is not necessarily fixed and a point that is identified as maximum in one thermal image may not remain the maximum as time progresses. Choosing a defect-free location also introduces subjectivity because the temperature profile along the surface varies considerably due to nonuniform heating. Furthermore, FRP composites are not homogeneous materials. Fiber patterns and matrix variation result in texture that will appear in the thermal images. The second method will reduce the influence of the variability, but the areas to be averaged still involve subjective choice.

In the current study, an alternative method for computing ΔT_{def} versus time is proposed. The first step in the procedure is to identify an area around a defect by drawing a rectangle directly on the thermal image. The width of the line defining the rectangle is one pixel. The primary requirement for the location of this rectangle is that the sides are located a

sufficient distance away from the defect. Figure 4 shows a properly defined area around Defect A75 on Specimen A-1.

After a rectangular area was defined for each defect, ΔT_{def} was computed at each time step using the following equation

$$\Delta T_{def} = T_{max} - T_{per\_avg} \quad (1)$$

where T_{max} is the maximum temperature bounded by the area and T_{per_avg} is the average temperature measured along the perimeter of the area.

Figure 5(a) provides a plot of T_{max} and T_{per_avg} versus time for the Defect A75 (flash heating). The corresponding ΔT_{def} versus time plot is provided in Fig. 5(b). Once this ΔT_{def} versus time plot was generated, the next step was to extract additional parameters from the plot that can be used to characterize the defect and the corresponding level of detection (Fig. 5(b)). ΔT_{max} is defined as the maximum value of ΔT_{def}, and t_{max} is the corresponding time at which the maximum value occurs.

A number of defects analyzed in this study produced markedly different thermal images and ΔT_{def} versus time plots. Figure 6 provides a series of thermal images for the interface bubble defect (IB) on Specimen A-3. The resulting ΔT_{def} versus time plot is provided in Fig. 7(a). This plot indicates a ΔT_{def} value of approximately 3.25 °C (5.8 °F) at t = 0 s. This signal slowly decays to a local minimum value of 2.5 °C (4.5 °F) at t = 12 s, and then the signal begins an upward trend until the absolute maximum value (ΔT_{max}) is reached at t = 40 s. A closer inspection of the thermal images taken at t = 0, 12, and 40 s helps to explain the ΔT_{def} versus time plot (Fig. 6). The false signal that occurs between t = 0 and t = 12 s is a result of minor imperfections in the FRP system and nonuniform heating of the specimen. At t = 12 s, there is a perceptible shift in the location of the maximum value toward the center of Defect IB. At t = 40 s, the dominant source of the ΔT_{def} signal is the defect of interest and the ΔT_{max} value has been achieved.

Another distinct ΔT_{def} versus time plot was generated for Defect E75 in Specimen A-3 (Fig. 7(b)). The plot begins with a false signal of 1.6 °C (2.9 °F) at t = 0 s due to nonuniform heating. The signal decreases with a near linear slope (plotted on a log scale) up to t = 15 s. There is no distinct local minimum to indicate precisely when the defect begins to dominate the signal. The thermal image did indicate that a defect was present, but the ΔT_{def} versus time plot offers no well-defined value for ΔT_{max}, t_{max}. The maximum temperature on the perimeter of the area boundary (T_{per_max}) was also recorded at each time step. Figure 7(c) provides a plot of T_{per_max} minus T_{per_avg} (labeled B in the figure). The data series labeled A is the original ΔT_{def} versus time plot. When Series B is subtracted from A, the resulting Curve C provides a clear indication of when the defect begins to dominate the signal.

A threshold value of 0.2 °C (0.36 °F) was chosen as the minimum ΔT_{max} for which a defect would be classified as

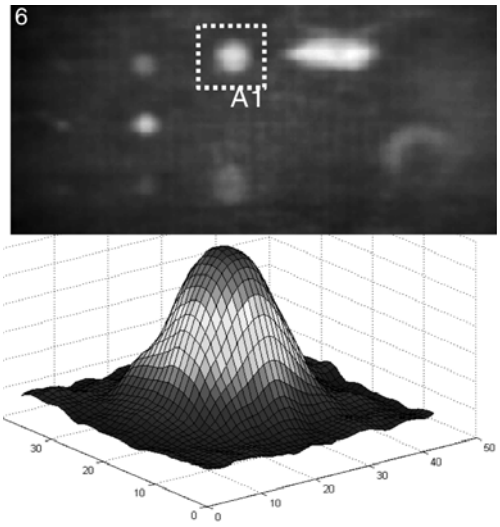

Fig. 4—Area identification for defect analysis (Defect A75, Specimen A-1). Thermal image and corresponding surface plot for properly defined defect area.

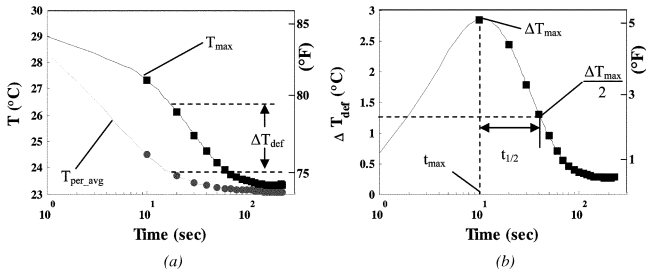

Fig. 5—Constructing ΔT_{def} versus time plots from area parameters. Defect A75, Specimen A-1 (flash heating): (a) T_{max} and T_{per_avg} versus time; and (b) ΔT_{def} versus time.

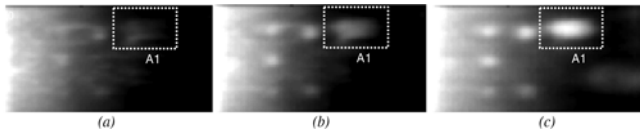

Fig. 6—Thermal images for Defect IB (Specimen A-3): (a) t = 0 s; (b) t = t_b (t = 12 s); and (c) t = t_{max} (t = 40 s).

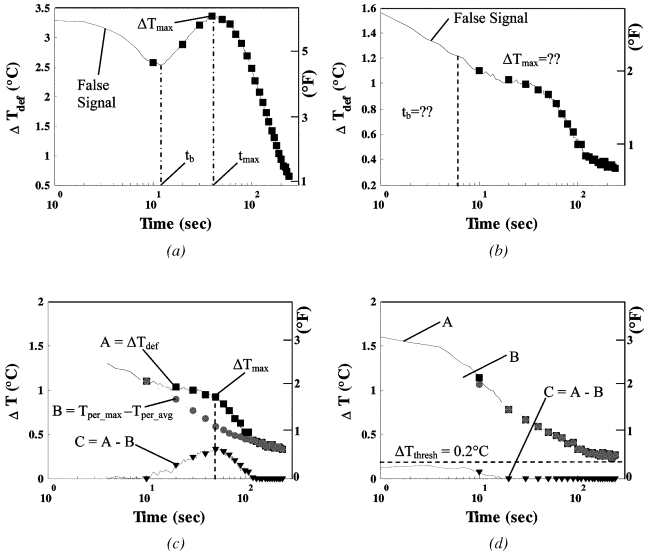

Fig. 7—Nonuniform heating and weak signals for defects: (a) ΔT_{def} versus time for Defect IB in Specimen A-3 (long-pulse heating – 45 seconds); (b) ΔT_{def} versus time for Defect E75 in Specimen A-3 (long-pulse heating – 45 seconds); (c) ΔT_{def} versus time for Defect E75 with perimeter difference removed; and (d) ΔT_{def} versus time for undetected defect (E50 in Specimen A-3, long-pulse heating – 45 seconds).

detected. If the maximum value obtained by Curve C is less than 0.2 °C (0.36 °F), the defect is considered to be undetected. Figure 7(d) provides an example of a ΔT_{def} versus time plot for an undetected defect (Defect E50 in Specimen A-3).

The interface bubble (IB), the 19 mm (0.75 in.) diameter air-filled hole (A75), and the 19 mm (0.75 in.) diameter epoxy-filled hole (E75) were chosen from each specimen to compare and contrast the ΔT_{max} values obtained for each heating method. A large value of ΔT_{max} is desirable in this application because it increases contrast for defects in thermal images and can reduce the effects of noise and nonuniform heating. Figure 8 provides a series of bar charts for the selected defects where the *x*-axis denotes the heating method and the *y*-axis denotes ΔT_{max} for the defect.

The factors that affect ΔT_{max} are numerous: size of the defect (*x*-*y* plane), defect depth, material composition of the defect, heat source intensity, and the duration of the heat pulse. The highest value of ΔT_{max} observed for Defect IB in Specimen A-1 was obtained using the scan heating method (18.8 °C [33.8 °F]). The pulse heating method resulted in the lowest value for ΔT_{max} (3.3 °C [5.9 °F]) (Fig. 8(a)).

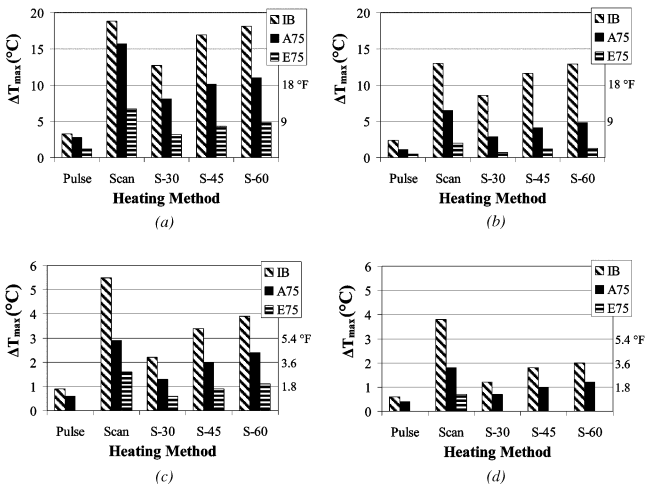

Fig. 8—Comparison of ΔT_{max} *for different heating methods: (a) Specimen A-1; (b) Specimen A-2; (c) Specimen A-3; and (d) Specimen A-4.*

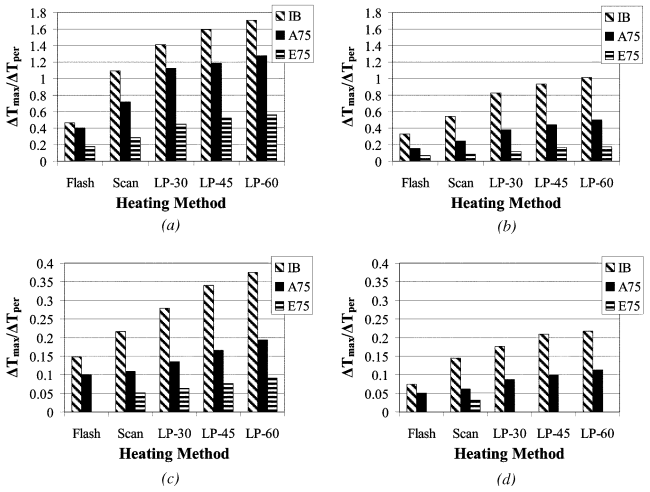

Fig. 9—Comparison of normalized ΔT_{max} *for different heating methods: (a) Specimen A-1; (b) Specimen A-2; (c) Specimen A-3; and (d) Specimen A-4.*

A similar trend was observed for the two-, three-, and four-layer specimens.

- The scan heating method produced the highest values for ΔT_{max};
- The smaller diameter defects produced lower ΔT_{max} values; and
- Epoxy-filled defects produced lower ΔT_{max} values.

The relatively high values for ΔT_{max} that were observed for the scan heating method resulted from the high intensity of the applied heat flux. Normalized ΔT_{max} ($\Delta T_{max}/\Delta T_{per}$) is a more useful parameter for investigating the effects of pulse duration on defect detectability. By dividing ΔT_{max} by the average temperature increase that was experienced by the perimeter of the defect boundary, the effects of heat flux intensity are removed. Normalized ΔT_{max} results for defects IB, A75, and E75 are provided in Fig. 9.

An important consideration for future studies relates to the defect layout pattern in the horizontal plane. A small degree of thermal interaction was observed between Defect IB and Defect A75 on Specimen A-3 (Fig. 6(d)) and Specimen A-4 (Fig. 10(b)). This indicates that these defects were originally positioned too close together. This interaction resulted in an increase in the temperature computed around the perimeter of the defect (T_{per_avg}) and the maximum temperature generated by the defect (T_{max}). The overall effect on ΔT_{max} cannot be determined, but there is a tendency for the resulting temperature increases to cancel out when ΔT_{max} is computed.

These data are insufficient to develop a mathematical relationship for normalized ΔT_{max} as a function of pulse duration, defect depth, defect size, and defect material composition. It is possible, however, to use these data to help determine how a particular FRP composite system should be inspected. Once a suitable ΔT_{max} value has been determined for a particular thermal imaging system, the normalized ΔT_{max} plots indicate the required ΔT_{per} that must be generated to develop this signal for a specific type of defect. For example, assume that an IRT inspection is going to be conducted on a 3 mm (0.12 in.) thick CFRP system and the smallest defect of interest is 19 mm (0.75 in.) in diameter. Also, assume that 2 °C (3.6 °F) is the desired value for ΔT_{max}. For a long-pulse heating setup with a 30-second pulse duration, the minimum required temperature increase for the defect-free area (ΔT_{per}) is 14.8 °C (26.6 °F). This quantity is obtained by dividing the desired ΔT_{max} by the normalized ΔT_{max} result for Defect A75 on Specimen A-3 (0.135 as shown in Fig. 9(c)). Once this quantity has been obtained, it becomes a matter of determining the appropriate lamp intensity and lamp configuration required to generate the 14.8 °C (26.6 °F) temperature increase.

Defect area computations

One method for determining the size of a defect (*x*-*y* plane) from a thermal image is to draw a line around the apparent boundary of the defect and count the number of pixels inside the boundary. The number of pixels can be converted to an area by applying a length factor based on two points of known separation. This procedure will be referred to as the boundary trace method. Figure 11(a) illustrates the boundary trace method applied to Defect A75 on Specimen A-1. The total number of pixels bounded by the trace was 377. After applying the length factor for this image (1.1 mm/pixel or 1.2 mm^2/pixel [0.043 in./pixel or 0.0019 $in.^2$/pixel]), the area of the defect was estimated to be 4.4 cm^2 (0.68 $in.^2$). The true area for this defect was 2.8 cm^2 (0.43 $in.^2$). Additional investigation into the boundary trace method

focused on results from the 60-second long-pulse heating experiment (Table 4). The camera configuration for this experiment resulted in an area factor for each pixel of 4.84 mm^2 (0.0866 in.^{2}). The percent error associated with these measurements indicates that the boundary trace method can over-predict the true defect area from 60 to 300% of the actual defect area. In general, the error associated with the boundary trace method increases as the thickness of the composite increases.

Selecting the boundary of the defect will always require some degree of human judgment. Maldague (2001) and Starnes et al. (2003) both outline a procedure for approximating the size of a defect by computing the magnitude of the maximum temperature gradient at the defect boundary in a thermal image. The underlying principle for this procedure is that the location of maximum slope of the temperature field corresponds to the edge of the defect below the surface. This procedure will be referred to as the gradient area method in the text below.

The gradient image generated for Defect A75 (Specimen A-1) is provided in Fig. 11(b). The defect boundary was determined by first identifying the pixel with the smallest gradient near the center of the defect. A line was constructed between the center and the upper left corner of the area containing the defect. The location of the maximum gradient value along this line was determined and stored as one point on the defect's boundary. Next, a new line is constructed from the center point to the pixel on the border just below the upper left pixel. The location of the maximum gradient is computed again and stored as the second point along the boundary of the defect. The process is repeated for a series of lines drawn from the center point to each pixel along the boundary of the area. Once this boundary has been determined, the number of pixels contained within the boundary is summed. The number of pixels can then be converted into physical units by scaling with an appropriate factor. The boundary trace method procedure resulted in a better estimate for the defect area for Defect A75 and Defect IB on Specimen A-1 than the boundary trace method (Fig. 11). The estimated area for Defect A75 using the flash heating setup was 2.6 cm^2 (0.40 in.^{2}) (actual area was 2.8 cm^2 [0.43 in.^{2}]) and the estimated area for Defect IB was 6.4 cm^2 (1.0 in.^{2}) (actual area was 7.1 cm^2 [1.1 in.^{2}]).

The results from the 60-second long-pulse heating experiment (Table 4) also support the idea that the gradient area method provides a better estimate for defect area. For well-defined, air-filled defects, this method produced results within ±15% of the actual defect area. The percent error associated with epoxy-filled defects was within ±30% of the actual defect area. The standard deviation for defect area was also computed using the results from the scan and the 30-, 45-, and 60-second heating methods. The standard deviation was within 5% of the average for Specimens A-1 and A-2 (with the exception of Defect IB in Specimen A-2) and within 20% for Specimens A-3 and A-4.

Results from the current study indicate several factors that can reduce accuracy in area computations using the gradient area method:

- Low ΔT_{max} for the defect;
- High temperature gradient due to nonuniform heating; and
- Insufficient pixel resolution for small defects.

Figure 10 provides three examples of defects that were clearly visible in thermal images but resulted in poor area estimates when the gradient area method was applied. The flash heating method generated a ΔT_{max} of 0.6 °C (1.1 °F) for Defect A75 in Specimen A-3. For this low value of ΔT_{max}, the natural variation in the composite's texture and noise in the thermal image tend to dominate the temperature gradient. The resulting gradient image for this defect does not provide a well-defined defect boundary (Fig. 10(a)).

Defect signals that occur in regions of nonuniform heating can also produce inaccurate gradient area results. Figure 10(b) provides a thermal and gradient image for Defect E75 in Specimen A-3 (30-second long-pulse heating). The area in which the nonuniform heating blends into the defect results in a region where the temperature gradient is essentially zero. The maximum temperature gradient in this region can be influenced by noise and produce a skewed defect boundary. The final source of error in the gradient area method was insufficient pixel resolution for small defects. The long-pulse setup generated a clearly visible signal for Defect A25 (6.4 mm [0.25 in.] diameter), but the associated pixel resolution for this image was only 2 mm/pixel [0.08 in./pixel]). The gradient image for this defect did develop what appears to be a valid defect boundary, but the location of the local maximum and minimum do not reflect the actual center point and boundary of the defect.

By computing the coefficient of variation (COV) of the radius values generated by the gradient area method, it was possible to quantify the quality of the defect boundary. The COV is defined as the standard deviation of a series of numbers divided by the mean value. When the gradient area

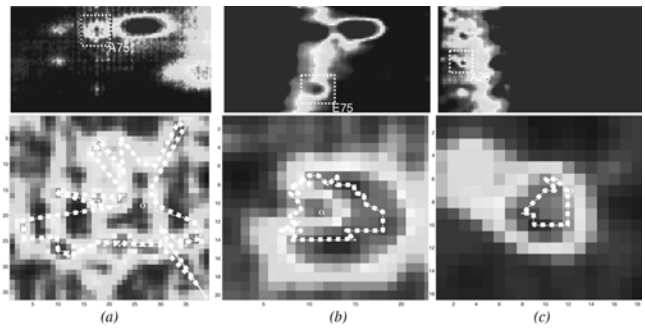

Fig. 10—Reduced accuracy in area computations due to: (a) weak signal; (b) nonuniform heating; and (c) insufficient pixel resolution.

Table 4—Actual and measured areas for select defects (60-second pulse heating)

		Area in pixels (actual/gradient method/boundary method)				
60-second pulse		IB	A75	A50	E75	E50
Layers	1	147/131/328	59/50/127	26/23/104	59/71/185	26/20/95
	2	267/235/440	59/52/159	26/34/112	59/76/177	26/*/183
	3	229/269/533	59/64/198	26/*/153	59/*/194	26/*/165
	4	264/260/661	59/*/216	26/*/161	59/*/247	26/*/123
Scan, 30-, 45-, and 60-second heating		Mean and (standard deviation) for gradient area in pixels (N = 4)				
		IB	A75	A50	E75	E50
Layers	1	133 (3.0)	49 (1.5)	22 (1.3)	67 (3.9)	21 (1.3)
	2	249 (13.0)	53 (1.3)	32 (4.1)	73 (4.1)	*
	3	268 (8.6)	73 (7.4)	*	*	*
	4	277 (19.7)	*	*	*	*

*Indicates that defect boundary was not sufficiently defined for gradient method.
Note: 1 pixel = 4.84 mm^2 (0.0075 in.^{2}).

method was applied to the defect shown in Fig. 10(a), a total of 152 radius values were obtained. The center point of this defect is labeled "o" and the COV for the radius values was 0.54. In contrast, the COV for the well-defined defect shown in Fig. 11(b) was 0.10.

Proposed method for characterizing detectability

The experiments conducted in this study resulted in a total of 140 ΔT_{def} versus time plots (seven defects in four specimens with five different heating procedures). To produce a sensible set of results that can be used to characterize defect detectability, a new classification procedure is proposed. The first distinction that will be made for each defect is based on the shape of the ΔT_{def} versus time plot. There were four basic shapes encountered in this study leading to a simple Level I, Level II, Level III, or Level IV classification system. Level I defects assume a positive slope for $t > 0$ and achieve a single maximum value at $t = t_{max}$ (Fig. 5(b)). Level II curves begin with a negative slope and reach a local minimum at $t = t_b$. After reaching the local minimum, the curve assumes a positive slope for $t > t_b$ until a distinct local maximum is reached at $t = t_{max}$ (Fig. 7(a)). Level III curves begin with a negative slope and never assume a positive slope (Fig. 7(b)). There is, however, a distinct t_b that is recognizable when the difference in temperature on the perimeter of the defect's

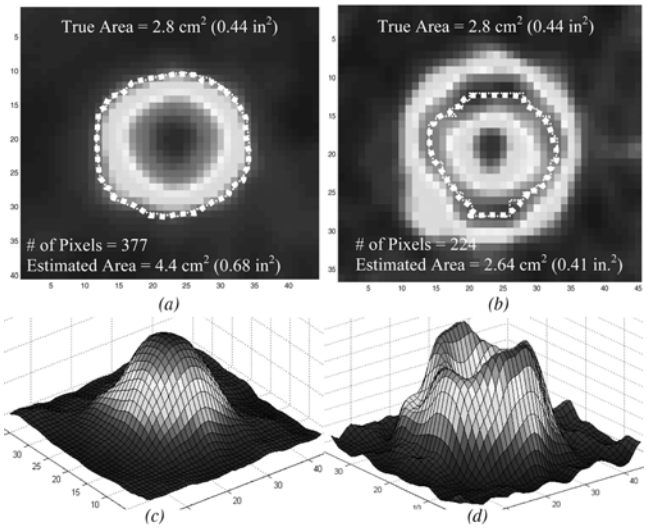

Fig. 11—Area computations for Defect A75: (a) boundary trace method; (b) gradient area method; (c) surface temperature profile; and (d) temperature gradient profile.

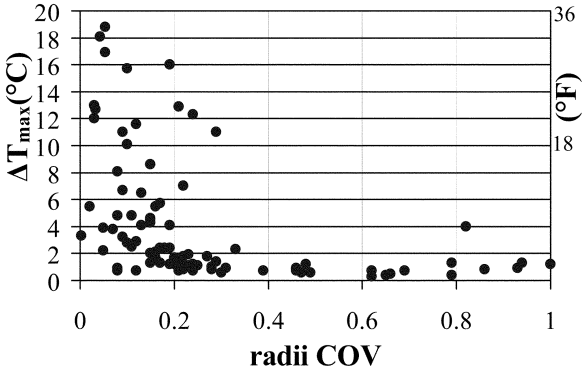

Fig. 12—Maximum signal versus radii COV for all detected defects.

defining area is subtracted from the ΔT_{def} versus time plot. This can also be recognized as an inflection point in the ΔT_{def} versus time plot. The final classification, Level IV, is intended to describe defects that were not detected (Fig. 7(d)).

The shape of the ΔT_{def} versus time curve is a very important indicator of defect detectability. Level I defects appear in thermal images immediately after the heat source is removed. The relative intensity of the defect hot spot is large enough that Level I defects are easily recognized. Level II defects also generate well-defined hot spots, but the time at which the maximum value occurs must be considered. For the 3 and 4 mm (0.12 and 0.16 in.) samples, the time of maximum defect signal strength ranged from 30 to 80 seconds (scan heating results). If thermal images are not recorded for a sufficient period of time after heating these defects can easily go undetected. The implications of a Level III classification are that the overall defect signal strength is low and the defect area is obscured by high temperature gradients due to nonuniform heating. Detecting Level III defects requires selective manipulation of the image color scale so the shape of the defect can be extracted from the thermal image (Fig. 10(b)). Finally, Level IV indicates a defect that could not be detected with the heating methods or thermal imaging system used in this study. It should be noted, however, that additional signal and image processing techniques are available that may allow the user to detect Level IV defects. These methods are beyond the scope of this paper.

A second distinction is made based on the COV of the computed radii of the defect using the gradient area method. A new quantity ΔCOV is introduced to describe the difference between the computed COV for the defect and the inherent COV for the shape of the defect. For circular defects, the computed COV and ΔCOV are equal because the inherent COV for a circle is zero. The inherent COV for an elliptical defect was obtained by considering the ratio of the ellipse radii for each IB defect (Table 2). Category A is intended for well-defined defects whose ΔCOV values are less than 0.21. Category B describes defects that are moderately defined by the gradient image and have ΔCOV values ranging between 0.21 and 0.4. Finally, Category C is for poorly defined defects whose ΔCOV values are between 0.41 and 1.0.

This classification system provides 12 unique categories to describe general defect detectability. Detectability is influenced by a number of factors: defect size, defect composition, defect depth below the surface, material properties of the composite, and the heating method employed during the inspection. This classification system will make it possible to discuss detectability from a broader perspective. For example, suppose that Defect E75 on Specimen A-3 was classified as Level III-C using the flash heating method. During the step-heating method with a 60-second pulse duration, however, the same defect was classified as a Level II-B. This would represent an improvement on the detectability scale.

General detectability results for all heating methods are summarized in Table 5. Flash heating for the single-layer carbon FRP system resulted in a Level I or Level II classification for all implanted defects. This indicates that a quantifiable signal was generated in the ΔT_{def} versus time plots for each defect. For the two-layer FRP composite system, all of the defects at least 12.7 mm (0.5 in.) in diameter or larger were considered Level I or Level II. The 6.4 mm (0.25 in.) diameter defects did not develop a significant signal in the ΔT_{def}

versus time plots. For the three-layer specimen, only air-filled defects with 12.7 mm (0.5 in.) diameters (or larger) developed a signal. Finally, only the IB and 19 mm (0.75 in.) diameter defect developed a significant signal in the four-layer specimen.

The data obtained from scan heating indicate an overall increase in detectability over the flash heating method. The scan heating method also resulted in higher classification levels based on the quality of the defect boundary. All defects were detected in Specimens A-1 and A-2. All defects except A25 and E25 were detected in Specimen A-3. Measurable signals were not obtained for the following defects in Specimen A-4: A50, A25, E50, and E25.

Long-pulse heating results indicate that pulse durations between 30 and 60 seconds have minimal influence on general detectability. For the single-layer specimen, all of the defects were detected in the ΔT_{def} versus time plots. The gradient images also produced well-defined boundaries for all defects except A25 and E25. For the two-layer specimen, all air-filled defects except A25 were detected in the plots and gradient images. Only epoxy-filled Defect E75 was detected in the plots and gradient images. For Specimen A-3, air-filled defects IB, A75 were detected in the plots and gradient images. Defect A50 and E75 developed very weak signals with a ΔT_{max} of 1.4 and 1.1 °C (2.5 and 2.0 °F), respectively. Defects A25, E50, and E75 were not detected. Finally, only defects IB and A75 were detected in the four-layer specimen.

One final observation regarding general detectability is related to ΔT_{max} and ΔCOV. Figure 12 provides a plot of ΔT_{max} versus radii ΔCOV for each of the detected defects. If all of the defects had been detected for each of the heating methods, this plot would contain a total of 140 data points. Because a number of defects were classified as "undetected," ΔT_{max} and ΔCOV values were only recorded for 92 points. These data indicate that high radii COV values are most likely to occur if ΔT_{max} is less than 2.0 °C (3.6 °F). If ΔT_{max} is greater than 2.0 °C (3.6 °F), the radii COV tends to be less than 0.2 (indicating a well-defined defect boundary). This observation has the potential of simplifying the detectability classification structure. Instead of 12 different detectability levels (four based on ΔT_{def} versus time plot characteristics and three based on radii COV), it may be more efficient to classify defects as follows:

- Well-defined defects have a $\Delta T_{max} > 2.0$ °C (3.6 °F); and
- Poorly defined defects have a $\Delta T_{max} < 2.0$ °C (3.6 °F).

CONCLUSIONS

Results from the current study indicate that IRT is a potentially useful tool for evaluating bond in FRP systems applied to concrete. This research investigated different heating methods and proposed a new classification system to characterize defect detectability. This classification system is based on the measured signal strength of a defect as a function of time and accounts for the effects of nonuniform heating. Emphasis was also placed on characterizing the quality of a specific defect boundary as it appears in a thermal image. The boundary of each defect was computed from a gradient image, and the resulting COV of the defect's radius was incorporated into the classification system. This approach suggests that there are several layers of defect detectability that range from very well defined to not defined. This proposed classification system may serve as a point of reference for future research and will hopefully facilitate the exchange of information as new procedures for performing IRT inspections are investigated and this method is applied to different FRP systems.

Table 5—General detectability results for flash heating

Flash heating detectability	Defect						
	IB	A75	A50	A25	E75	E50	E25
Layers	I-A	I-A	I-A	II-B	I-A	II-A	II-C
	I-A	II-B	II-A	IV-C	II-C	II-C	IV-C
	II-A	II-C	II-C	IV-C	IV-C	IV-C	IV-C
	II-B	II-C	IV-C	IV-C	IV-C	IV-C	IV-C
Scan heating detectability	Defect						
	IB	A75	A50	A25	E75	E50	E25
Layers	I-A	I-A	I-B	I-C	I-A	I-A	I-B
	I-A	I-A	II-A	II-B	II-A	II-B	II-C
	II-A	II-A	II-A	IV-C	III-A	III-B	IV-C
	II-A	II-B	IV-C	IV-C	III-B	IV-C	IV-C
30-second pulse	Defect						
	IB	A75	A50	A25	E75	E50	E25
Layers	I-A	I-A	I-A	I-C	I-A	I-A	I-C
	I-A	I-A	I-B	IV-C	II-B	III-C	IV-C
	II-A	II-A	III-B	IV-C	III-C	IV-C	IV-C
	II-B	II-C	IV-C	IV-C	IV-C	IV-C	IV-C
45-second pulse	Defect						
	IB	A75	A50	A25	E75	E50	E25
Layers	I-A	I-A	I-A	I-C	I-A	I-A	I-C
	I-A	I-A	I-A	IV-C	II-A	II-C	IV-C
	II-A	II-A	III-B	IV-C	III-B	IV-C	IV-C
	II-B	II-B	IV-C	IV-C	IV-C	IV-C	IV-C
60-second pulse	Defect						
	IB	A75	A50	A25	E75	E50	E25
Layers	I-A	I-A	I-A	I-C	I-A	I-A	I-C
	I-B	I-A	I-B	IV-C	II-A	IV-C	IV-C
	II-A	II-A	III-B	IV-C	III-B	IV-C	IV-C
	II-A	II-C	IV-C	IV-C	IV-C	IV-C	IV-C

It was shown that defects as small as 6.4 mm (0.25 in.) in diameter can be detected in 1 mm (0.04 in.) thick CFRP composites. For the thickest CFRP composite systems investigated in the current study (4 mm [0.16 in.]), defects as small as 19 mm (0.75 in.) in diameter were detected. Flash heating was effective for detecting air-filled defects in single-layer (1 mm [0.04 in.]) CFRP systems. Defects larger than 12.8 mm (0.5 in.) in diameter developed a strong signal ($\Delta T_{max} > 2.0$ °C [3.6 °F]) that could be used to estimate size. Flash heating produced weak signals for implanted defects in CFRP systems 2 mm (0.08 in.) thick or greater. Scan heating was effective for detecting air-filled and epoxy-filled defects in CFRP systems up to 4 mm (0.16 in.) thick. Scan heating also produced higher values for ΔT_{max} compared with flash and long-pulse heating. Long-pulse heating was also effective for detecting air- and epoxy-filled defects that occurred up to 4 mm (0.16 in.) beneath the surface. One disadvantage of the long-pulse method was that the surface was not heated uniformly.

The ultimate decision about which heating method should be used for a specific IRT inspection will still vary depending on the desired objectives. Additional quantitative analysis procedures can be applied to IRT data for the purposes of further characterizing detected defects (that is, depth below the surface and material composition). This

study represents a useful first step in distinguishing which types of defects might be considered for further analysis as well as which defects are likely to be detected at all.

ACKNOWLEDGMENTS

The authors would like to acknowledge the support provided by the Florida Department of Transportation. This material is based upon work supported under a National Science Foundation Graduate Research Fellowship.

REFERENCES

ACI Committee 440, 2002, "Design and Construction of Externally Bonded FRP Systems for Strengthening Concrete Structures (ACI 440.2R-02)," American Concrete Institute, Farmington Hills, MI, 45 pp.

Avdelidis, N. P.; Almond, D. P.; Dobbinson, A.; Hawtin, B.; Ibarra-Castanedo, C.; and Maldague, X. P., 2004, "Thermal Transient Thermographic NDT and E of Composites," Proceedings of SPIE, *Thermosense XXVI*, D. D. Burleigh, E. Cramer, G. R. Peacock, eds., V. 5405, pp. 403-413.

Bai, W., and Wong, B. S., 2001, "Photothermal Models for Lock-In Thermographic Evaluation of Plates with Finite Thickness under Convection Conditions," *Journal of Applied Physics*, V. 89, No. 6, pp. 3275-3282.

Brown, J. R., and Hamilton, H. R., III, 2004, "NDE of Fiber-Reinforced Polymer Composites Bonded to Concrete Using IR Thermography," *Thermosense XXVI*, D.D. Burleigh, E. Cramer, G. R. Peacock, eds., Proceedings of SPIE, V. 5405, pp. 414-424.

Carlomagno, G. M., and Meola, C., 2002, "Comparison between Thermographic Techniques for Frescoes NDT," *NDT&E International*, V. 35, No. 8, pp. 559-565.

Civil Engineering Research Foundation, 2001, "Gap Analysis for Durability of Fiber-Reinforced Polymer Composites in Civil Infrastructure," CERF, Reston, VA, pp. 121-124.

Ibarra-Castanedo, C., and Maldague, X. P., 2005, "Pulsed Phase Thermography Inversion Procedure Using Normalized Parameters to Account for Defect Size Variations," *Thermosense XXVII*, Proceedings of SPIE, D. D. Burleigh, E. Cramer, and J. Miles, eds., V. 5782, pp. 334-341.

ICC Evaluation Services, 2003, "Acceptance Criteria for Concrete and Unreinforced Masonry Strengthening Using Fiber-Reinforced Composite Systems," AC125, Whittier, CA, p. 7.

Kaiser, H., and Kharbari, V., 2001, "Quality and Monitoring of Structural Rehabilitation Measures (Part I: Description of Potential Defects)," *Report* Contract No. 18347, Oregon Department of Transportation, p. 39.

Kharbari, V. M.; Chin, J. W.; Hunston, D.; Benmokrane, B.; Juska, T.; Morgan, R.; Lesko, J. J.; Sorathia, U.; and Reynaud, D., 2003, "Durability Gap Analysis for Fiber-Reinforced Polymer Composites in Civil Infrastructure," *Journal of Composites for Construction*, V. 7, No. 3, pp. 238-247.

Kulowitch, P. J.; Perez, I. M.; and Granata, D., 1995, "Flash Infrared Thermography for Nondestructive Testing (NDT) I/E of Naval Aircraft," *Thermosense XVI*, Proceedings of SPIE, S. A. Semanovich, ed., V. 2473, pp. 252-262.

Levar, J. M., and Hamilton, H. R., 2003, "Nondestructive Evaluation of Carbon Fiber-Reinforced Polymer-Concrete Bond Using Infrared Thermography," *ACI Materials Journal*, V. 100, No. 1, Jan.-Feb., pp. 63-72.

Maldague, X. P. V., 2001, *Theory and Practice of Infrared Technology for Nondestructive Testing*, John Wiley & Sons, Inc., 704 pp.

Maldague, X.; Galmiche, F.; and Ziadi, A., 2002, "Advances in Pulsed Phase Thermography," *Infrared Physics and Technology*, V. 43, No. 3-5, pp. 175-181.

Mirmiran, A.; Shawhawy, M.; Nanni, A.; and Kharbari, V., 2004, "Bonded Repair and Retrofit of Concrete Structures Using FRP Composites," *Report* 514, National Cooperative Highway Research Program, Washington, D.C., pp. II-27 to II-28.

Nanni, A., 2003, "North American Design Guidelines for Concrete Reinforcement and Strengthening Using FRP: Principles, Applications and Unresolved Issues," *Construction and Building Materials*, V. 17, No. 6-7, pp. 439-446.

Starnes, M. A.; Carino, N. J.; and Kausel, E. A., 2003, "Preliminary Thermography Studies for Quality Control of Concrete Structures Strengthened with Fiber-Reinforced Polymer Composites," *Journal of Materials in Civil Engineering*, V. 15, No. 3, pp. 266-273.

Starnes, M. A., and Carino, N. J., 2005, "Active Infrared Thermography for NDT of Concrete Structures Strengthened with Fiber-Reinforced Polymer," *Journal of Materials Evaluation*, Jan., pp. 56-63.